Performance Assessment of Simulated CYGNSS Measurements in the Tropical Cyclone Environment

Faozi Saïd, *Member, IEEE*, Seubson Soisuvarn, *Member, IEEE*, Zorana Jelenak, *Member, IEEE*, and Paul S. Chang, *Member, IEEE*

***Abstract*—The capability of the cyclone global navigation satellite system (CYGNSS) to observe winds within tropical cyclones (TCs) is assessed by using simulated CYGNSS observations over 43 cyclones from 2010 to 2011. The CYGNSS end-to-end simulator (E2ES) is utilized to generate delay-Doppler maps from which wind speeds are then retrieved. These wind speeds are first compared to the high-resolution model winds input into the E2ES. For range corrected gain (RCG) values greater than 20, the CYGNSS winds have a standard deviation of 0.57 m/s relative to these model winds. An error probability lookup table is developed to improve performance for RCG values lower than 20, as well as minimizing data loss (up to 4.4%). Since actual TCs are utilized in this study, the CYGNSS winds are also compared to winds from the advanced SCATterometer (ASCAT), the Oceansat-II scatterometer, GPS dropsondes, the stepped frequency microwave radiometer, and the H*wind model analysis. The CYGNSS winds compared best to the ASCAT winds with an overall bias around −0.4 m/s, and a standard deviation less than 1.54 m/s. GPS dropsonde winds compared less favorably with a standard deviation around 7.36 m/s, which can be partially attributed to spatial and temporal sampling differences. The CYGNSS ability to retrieve the TC maximum wind is also evaluated using the national hurricane center best track maximum winds. Although the CYGNSS overall bias varied from season to season (from −4.7 m/s in the Atlantic basin-2011 to −13.0 m/s in the Atlantic basin-2010), the standard deviation remained fairly consistent.**

***Index Terms*—Geophysical measurements, global positioning system, microwave reflectometry, radar measurements, remote sensing, scattering, sea surface, wind.**

I. Introduction

THE ability to retrieve sea surface winds under tropical cyclone (TC) conditions is an on-going challenge. *In-situ* measurements from buoys, GPS dropsondes, and remotely sensed measurements from microwave instruments (e.g., scatterometers, radiometers, synthetic aperture radars) are routinely used to retrieve sea surface winds under a variety of environmental conditions [1]–[6]. Sea surface reflected signals from the global navigation satellite systems (GNSS) have also shown correlation to the wind signal on the ocean surface [7], [8]. This remote sensing technique is commonly referred to as GNSS Reflectometry (GNSS-R), where a GNSS receiver generates a delay-Doppler map (DDM) at specular points on the ocean surface [see Fig. 1]. The wind speed can then be inferred from the measured DDM via an inversion procedure [9]–[12]. The UK-DMC-1, launched on September 23rd 2003, was the first spaceborne earth observation satellite which successfully collected DDM measurements [11]. Although very limited in nature (only 40 specular points were collected over the ocean), this dataset revealed that the GNSS-R technique could be utilized from space. On July 8, 2014, TechDemoSat-1 was launched carrying the Space GNSS receiver-remote sensing instrument (SGR-ReSI) [13]. Although TechDemoSat-1 was launched as a technology risk reduction mission, significantly more DDM measurements were collected by the SGR-ReSI, from which sea surface wind speeds were successfully retrieved [14].

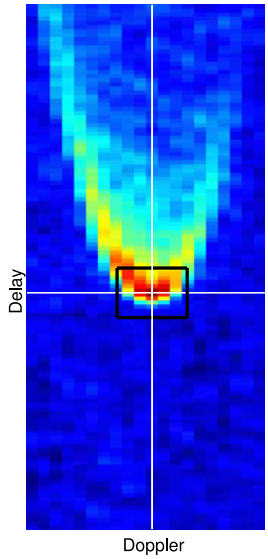

Fig. 1. Example of a DDM, including a DDMA represented by the black rectangle around the specular point.

The cyclone global navigation satellite system (CYGNSS), planned for launch in October 2016, represents the first dedicated GNSS-R satellite mission specifically designed to retrieve ocean surface wind speeds in the TC environment [15], [16]. CYGNSS will use a constellation of eight microsatellite observatories that can receive both the direct and reflected signals from GNSS. These observatories are capable of collecting four simultaneous reflections each, thus providing high temporal-resolution wind speed retrievals within TCs. In preparation for

Manuscript received September 16, 2015; revised February 18, 2016; accepted April 12, 2016. Date of publication May 31, 2016; date of current version October 14, 2016. This work was supported in part by the NASA CYGNSS project (NASA Science Mission Directorate Contract NNL13AQ00C) and the NOAA Ocean Remote Sensing Program.

F. Saïd is with the Sci-Tech II, Global Sciences & Technology, Greenbelt, MD 20770 USA (e-mail: faozi.said@noaa.gov).

S. Soisuvarn, Z. Jelenak, and P. S. Chang are with the Center for Satellite Applications and Research, National Oceanic and Atmospheric Administration, College Park, MD 20740 USA (e-mail: seubson.soisuvarn@noaa.gov; zorana.jelenak@noaa.gov; paul.s.chang@noaa.gov).

Color versions of one or more of the figures in this paper are available online at http://ieeexplore.ieee.org.

Digital Object Identifier 10.1109/JSTARS.2016.2559782

1939-1404 © 2016 IEEE. Personal use is permitted, but republication/redistribution requires IEEE permission.
See http://www.ieee.org/publications_standards/publications/rights/index.html for more information.

the CYGNSS mission, a simulator was developed to produce large sets of DDMs from CYGNSS observatory orbits [17]. A forward model was also developed to infer wind speeds from the simulated DDMs [18]. These tools are critical in assessing the CYGNSS potential performance in retrieving wind speed from TCs, as well as better understanding the mission strengths and weaknesses. In this paper, we assess the forward model performance from [18] (see Section II), and compare the simulated CYGNSS retrieved winds in TC conditions to the winds from the advanced SCATterometer (ASCAT) [19], the Oceansat-II scatterometer [20], GPS dropsondes [1], the stepped frequency microwave radiometer (SFMR) [21]), and the H*wind model analysis [22] (see Section III). Section IV provides a conclusion including possible future works.

II. Forward Model Evaluation

A. Description

Ocean surface wind retrievals from CYGNSS observables are made possible using a specially developed geophysical model function (GMF) that relates these observables to the ocean surface winds. A 13-day nature run dataset capturing the full life cycle of a TC [23], along with the CYGNSS end-to-end simulator (E2ES) [17], are used to generate the CYGNSS GMF. Ocean and atmosphere state variables from the nature run, including wind direction, wind speed, rain rate, freezing height, and surface permittivity, are used as inputs to the E2ES. The wind field is used to compute the mean square slope of the ocean surface, which in turn is used to calculate the L-band radar cross-section of the ocean surface, and ultimately the scattered power. The current implementation of the E2ES excludes sea surface wave related parameters, sea surface temperature, and ocean surface salinity. These additional geophysical parameters may be included in a future version of the simulator.

Using the E2ES, a large set of DDMs can then be generated. From each DDM, a DDM average (DDMA) and a leading-edge-slope (LES) are estimated. The DDMA represents an average of a DDM over a given delay/Doppler range window around the specular point (see Fig. 1); the LES refers to the slope of the leading edge of the integrated delay waveform [24]. The GMF is trained using wind speeds from 0–55 m/s on a 25 km $\times$ 25 km spatial grid, for incidence angles between 0° and 80°, and a receiver antenna gain greater than 15 (numeric). Fig. 2 shows both the DDMA and LES versus wind speed for various incidence angles. This figure shows that, given an incidence angle, a measured DDMA (or LES) leads to a unique wind speed. However, the steep and small slopes on the curves require accurate knowledge of the DDMA and LES to properly retrieve corresponding wind speeds.

Once wind speeds are retrieved from both the DDMA and LES observables, they are combined to generate a minimum variance (MV) estimator

$$U_{10}^{\mathrm{MV}} = k_0 U_{10}^{\mathrm{DDMA}} + k_1 U_{10}^{\mathrm{LES}} \tag{1}$$

where U_{10}^{MV} represents the final retrieved wind speed obtained from the MV estimator, U_{10}^{DDMA} is the wind speed retrieved from the DDMA observable, and U_{10}^{LES} is the wind speed retrieved from the LES observable [18]. The coefficients k_0 and k_1 used in (1) vary depending on the range corrected gain (RCG–see the appendix for additional details on this variable)

$$\begin{array}{lll} k_0 = 1 & k_1 = 0 & 1 < RCG < 3 \\ k_0 = 0.588 & k_1 = 0.412 & 3 < RCG < 5 \\ k_0 = 0.671 & k_1 = 0.329 & 5 < RCG < 10 \\ k_0 = 0.701 & k_1 = 0.299 & 10 < RCG < 20 \\ k_0 = 0.689 & k_1 = 0.311 & RCG > 20. \end{array} \tag{2}$$

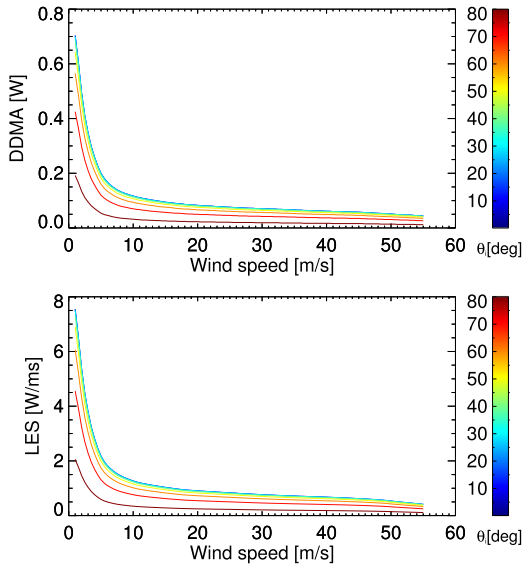

Fig. 2. Plots of CYGNSS observables relative to wind speed for various incidence angles using the CYGNSS GMF.

TABLE I
Tropical Cyclone Type Breakdown Per Basin-2010–2011 Seasons

	Tr. Dep.	Tr. Stor.	H. cat1	H. cat2	H. cat3	H. cat4
Atl.	1	14	3	0	3	6
Pac.	3	3	4	1	1	4
Total	4	17	7	1	4	10

B. Performance

The forward model is evaluated using realistic high-resolution model wind fields from the hurricane weather research model (HWRF) [25]. The 2010–2011 hurricane seasons from both the Atlantic (ATL) and Eastern Pacific (EPAC) basins are selected, yielding a total of 43 TCs. Table I shows the storm type breakdown per basin. The HWRF data is provided every 3 h throughout the life of a given TC. Additionally, three spatial resolution grids are available centered around the TC: 3, 9, and 27 km. While the 3- and 9-km resolution grids provide more detailed wind field characteristics in the immediate vicinity of the TC, the 27 km resolution grid covers a much larger spatial area [see Fig. 3(a)]. For each HWRF forecast cycle for each storm, the three corresponding HWRF resolution products are input into the E2ES to generate a series of DDMA and LES

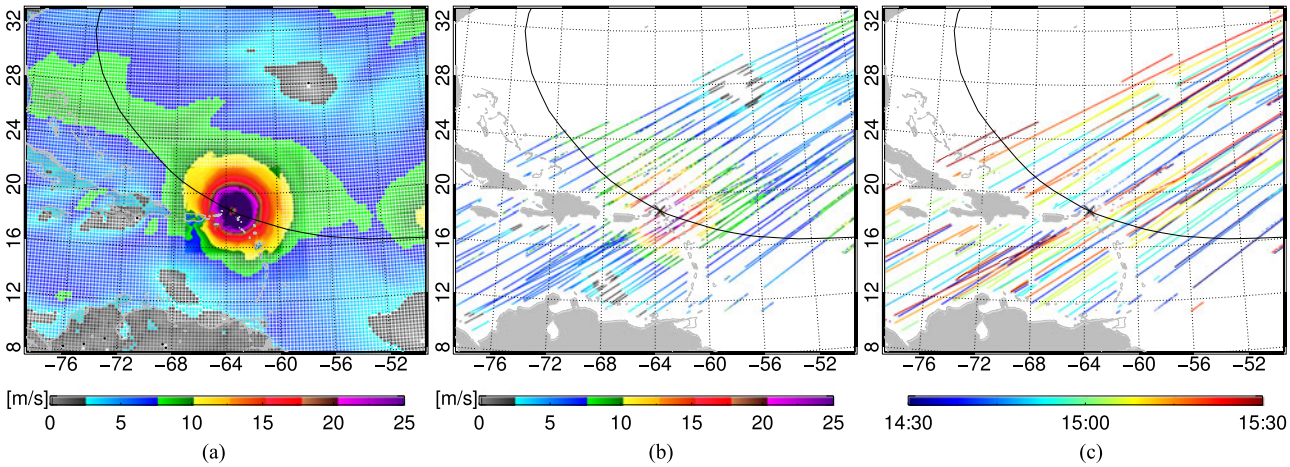

Fig. 3. Above plots show an HWRF pass over hurricane Earl on 30 August 2010 at 1500z (plot a), and CYGNSS passes over the same storm on the same date between 1430z and 1530z (see plot b). Since CYGNSS will use a constellation of eight microsatellites, plot c shows how CYGNSS passes occur over time between 1430z and 1530z. The plot of the HWRF pass features both the 3 and 27 km resolution grids. Finally, best track storm track and eye location (at 1500z) are also overlaid on all three plots.

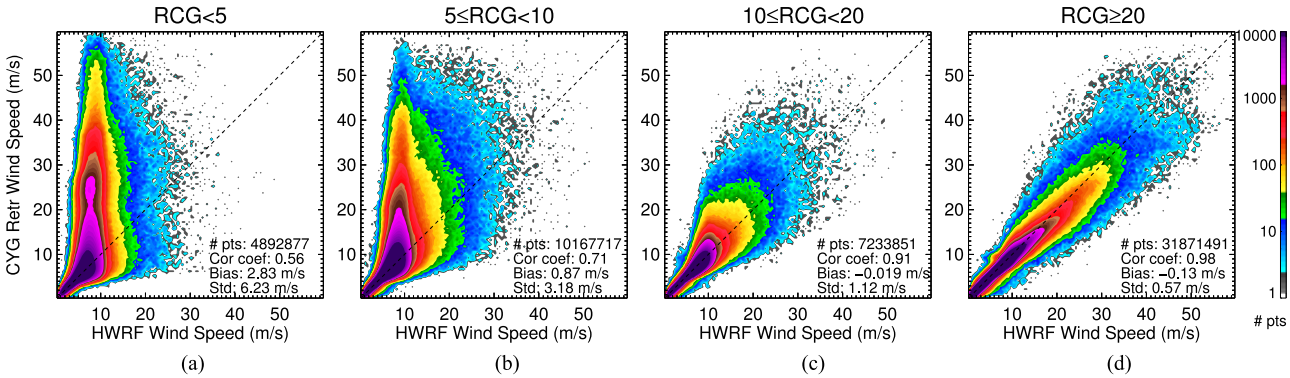

Fig. 4. Scatterplots of unfiltered simulated CYGNSS vs. HWRF wind speed for four different RCG ranges. High correlation exists for RCG greater than 10, whereas poor results are obtained for RCG less than 10 which represents about 28% of the whole dataset.

observables for each of the 43 storms. The GMF is then used to infer the wind speed from these simulated CYGNSS observables. As an illustration, Fig. 3(b) shows simulated CYGNSS retrieved winds for hurricane Earl (ATL basin) on 30 August, 2010 between 1430 z and 1530 z; Fig. 3(a) shows the corresponding HWRF storm snapshot on 30 August 2010 at 1500z. Since CYGNSS will use a constellation of eight microsatellite observatories, a storm pass can occur over a fairly large time span; in fact, Fig. 3(c) shows how the various CYGNSS passes happen over time between 1430 z and 1530 z on 30 August 2010 over hurricane Earl. This sampling is in contrast with a traditional scatterometer storm measurement swath, which would typically cover the entire area at essentially the same time.

Fig. 4 shows scatterplots of simulated CYGNSS versus HWRF wind speed for four different RCG ranges for all 43 TCs from Table I. For RCG values greater than 10, there is good overall agreement between the two datasets; for RCG values less than 10, a noticeable number of points show overestimated retrieved CYGNSS wind speeds. In Fig. 5, the wind speed bias and standard deviation between the CYGNSS retrieved winds and HWRF winds are plotted against the RCG and incidence angle values; a density plot [see Fig. 5(c)] is also included which shows that the majority of retrieved CYGNSS winds are retrieved at moderate to high incidence angles (i.e., 30°–70°), and with RCG values less than 50. The wind speed bias and standard deviation plots from Fig. 5 show good performance for all incidence angles and RCG values greater than 10.

C. Quality Flag Implementation

The final step in the retrieval process utilizes the MV algorithm to minimize the RMS error in the U_{10}^{DDMA} and U_{10}^{LES} wind speed estimates. Given the nature of the GMF (as shown in Fig. 2), a small change in either the DDMA or LES observables for wind speeds greater than ∼10 m/s, translates to relatively large range of wind speeds. Additionally, the signal-to-noise ratio can deteriorate as the RCG gets low. This can result in large discrepancies in the U_{10}^{DDMA} and U_{10}^{LES} wind speed estimates as shown in the scatterplots of Fig. 6(a) and (b). This large variability of U_{10}^{DDMA} and U_{10}^{LES} observables at low RCG values impacts the final wind speed retrieval output of the MV algorithm. In order to improve the wind retrieval performance

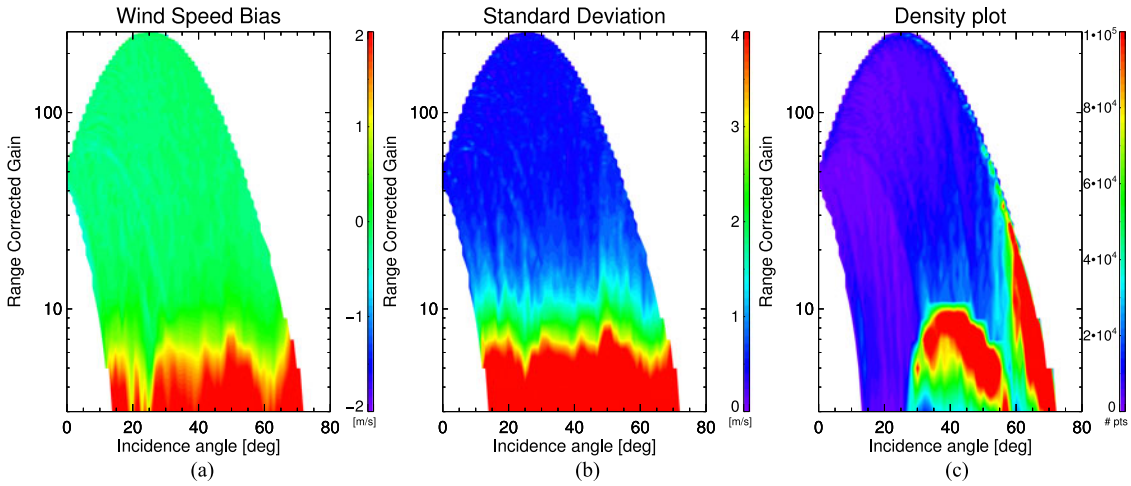

Fig. 5. Distributions of wind speed bias and standard deviation as a function of RCG and incidence angle (plots a and b). Plot c shows the density of points in terms of both RCG and incidence angle. We note a high concentration of points for RCG less than 25 and incidence angle greater than 30. Poor statistical results are obtained for very low RCG and for all incidence angles.

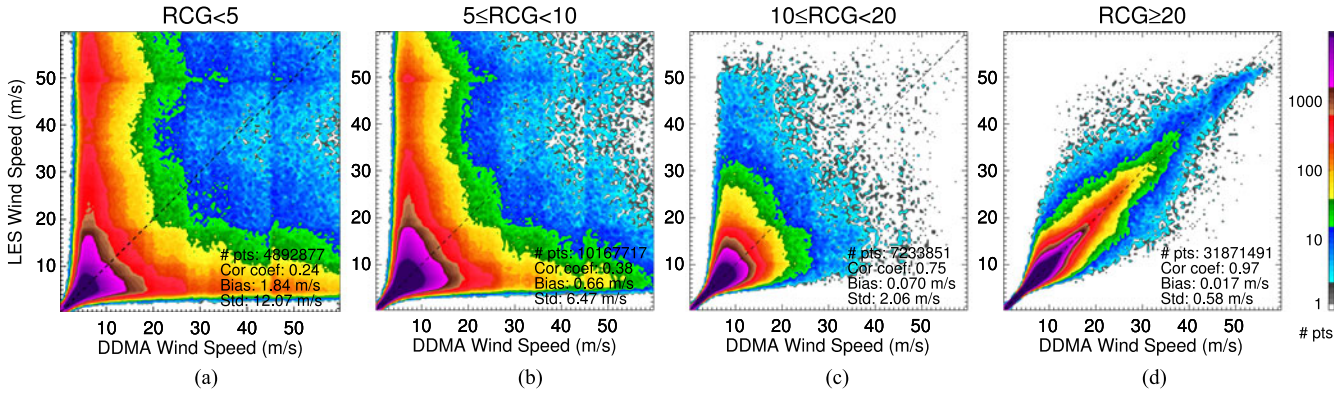

Fig. 6. Two-dimensional histograms of the distribution of U_{10}^{DDMA} vs. U_{10}^{LES} for four RCG ranges. These plots show that the error between these two variables decreases as the RCG increases.

across all RCG and incidence angle values while retaining as many retrievals as possible, a quality flag is developed and implemented to filter unrealistic retrievals. An error probability lookup table is therefore built as follows:

$$p_{\mathrm{err}}(|U_{10}^{\mathrm{MV}} - U_{10}^{\mathrm{HWRF}}| > 2 \Big| \{U_{10}^{\mathrm{DDMA}}, U_{10}^{\mathrm{LES}}, \mathrm{RCG}_{\mathrm{range}}\}) \quad (3)$$

where U_{10}^{HWRF} represents the HWRF wind speed, and $\mathrm{RCG}_{\mathrm{range}}$ correspond to four selected ranges of RCG

$$\begin{aligned} \mathrm{RCG} &< 5, \\ 5 \leq \mathrm{RCG} &< 10, \\ 10 \leq \mathrm{RCG} &< 20, \\ \mathrm{RCG} &\geq 20. \end{aligned} \quad (4)$$

A wind speed bin size of 0.5 m/s is used for wind speeds ranging from 0 to 60 m/s. The complete 2010-11 ATL and EPAC HWRF database is utilized to train the lookup table. Fig. 7 shows the error probability in terms of both U_{10}^{DDMA} and U_{10}^{LES} for the four selected RCG ranges. For RCG values less than 10, the likelihood of large wind speed bias (i.e., $|U_{10}^{\mathrm{MV}} - U_{10}^{\mathrm{HWRF}}| > 2$) is high when both U_{10}^{DDMA} and U_{10}^{LES} are greater than 15 m/s; for RCG values larger than 10, large wind speed bias is more likely to occur when U_{10}^{DDMA} and U_{10}^{LES} differ greatly from each other.

Various error probability thresholds are selected to determine optimal flagging conditions of the CYGNSS retrieved winds. Fig. 8 shows the bias and standard deviation between the CYGNSS and HWRF wind speeds versus averaged wind speeds for 50%, 70%, and 90% thresholds. As expected, unsatisfactory results are obtained when no quality flag is applied to the dataset [see Fig. 8(a)]. Once the quality flag is applied (e.g., 90% and 70% thresholds), the statistical results improve dramatically, albeit with a noticeably large bias for high winds. With a 50% threshold, the bias and standard deviation degrade for wind speed greater than 25 m/s. We find optimal performance, when compared to the CYGNSS baseline science requirements is obtained with an error probability threshold of 70% [see Fig. 8(c)]. This threshold is selected for all subsequent analysis presented in this paper.

Fig. 9 shows the same series of plots as in Fig. 5, but with the quality flag applied. The bias and standard deviation improvements are clearly noticeable in Fig. 9(a) and (b), particularly at

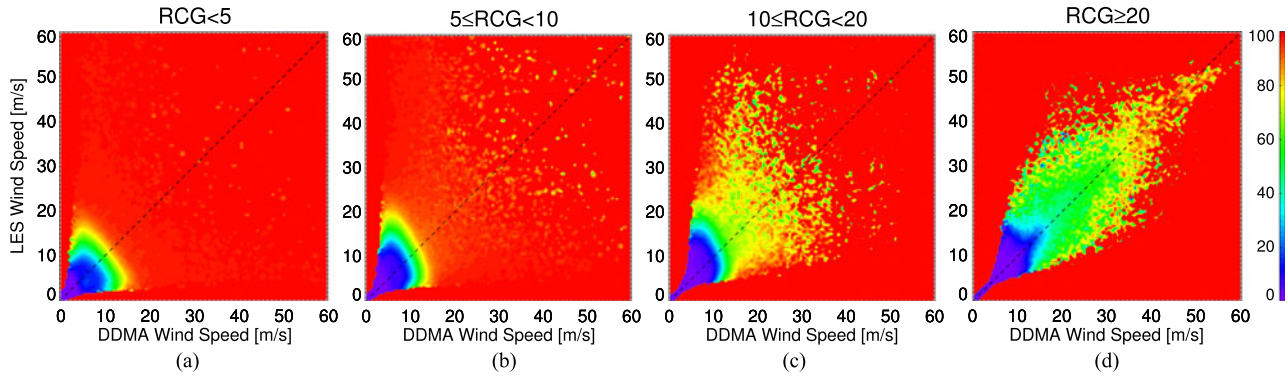

Fig. 7. Plots of the error probability relative to U_{10}^{DDMA} and U_{10}^{LES} for four RCG ranges. Plots a and b indicate that simulated CYGNSS winds should almost be completely flagged out when both U_{10}^{DDMA} and U_{10}^{LES} are greater than 15–20 m/s and RCG is less than 10. As the RCG increases however (see plots c and d), the error probability becomes lower for a wider range of U_{10}^{DDMA} and U_{10}^{LES}.

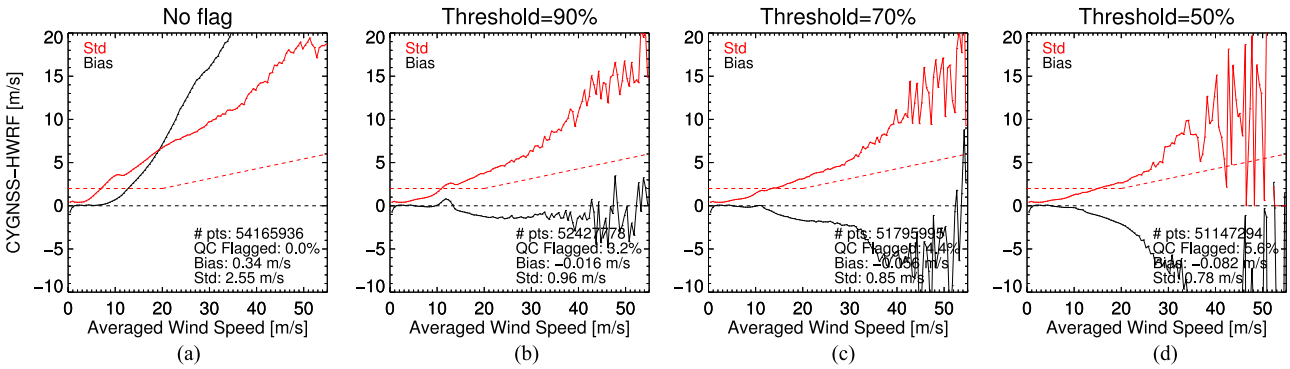

Fig. 8. Bias and standard deviation between simulated CYGNSS and HWRF wind speeds versus averaged wind speed, using various error probability thresholds. Although the curves are noisy above 40 m/s (0.01% of all retrieved wind speed samples are found in that range), best overall statistical results are obtained using a 70% threshold when compared to the CYGNSS science baseline requirements shown with the dashed lines.

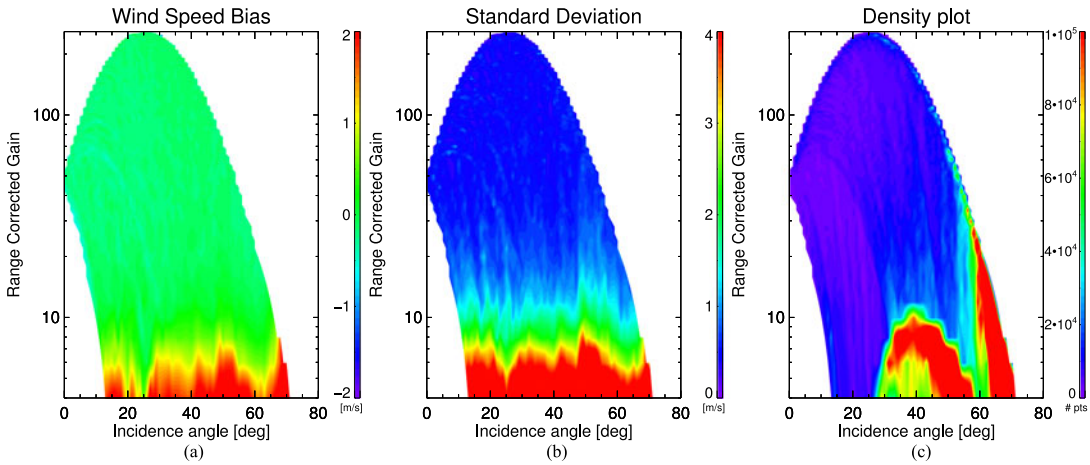

Fig. 9. Figure is a repeat of Fig. 5 except that the simulated CYGNSS data is now flagged. Wind speed bias and standard deviation distributions between simulated CYGNSS and HWRF wind speeds are shown in plots a and b, as a function of RCG and incidence angle; density of points is also shown in plot c as a function of RCG and incidence angle.

low RCG values. In order to improve the performance at moderate to high winds, a bias correction is also developed, using a "PDF matching" technique, and implemented in addition to the quality flag; this bias correction method is a fairly common technique used in the literature for GMF development [26]. This technique modifies the PDF of the CYGNSS wind retrievals to provide optimum correlation with the PDF of the HWRF winds, which are considered the truth winds in this case. The biases in the PDF of the CYGNSS wind retrievals can be caused by deficiencies in the GMF and wind retrieval methodology. Fig. 10(a) shows the PDFs of the CYGNSS, HWRF, and bias corrected CYGNSS winds; Fig. 10(b) plots the actual bias correction used. Fig. 10(c) shows the bias and standard deviation between the CYGNSS and HWRF winds as a function of the averaged

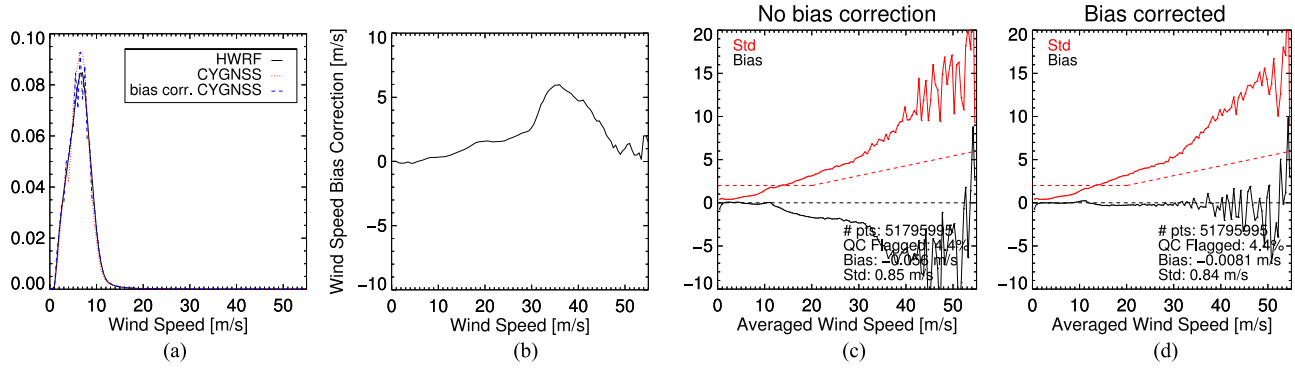

Fig. 10. Bias correction related plots. Plot a shows the pdf of CYGNSS with flag applied, HWRF, and bias corrected CYGNSS winds with flag applied. Plot b shows the amount of bias correction applied to the CYGNSS data in terms of wind speed. Plot c and d show the bias and standard deviation between flagged CYGNSS and HWRF winds, as a function of averaged wind speed, with and without bias correction applied.

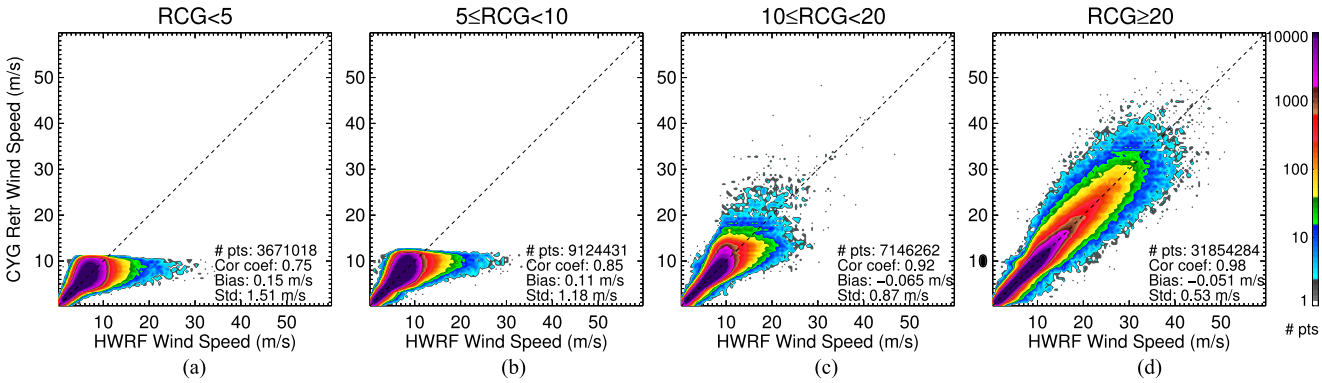

Fig. 11. Repeat of Fig. 4 but with both the flag and bias correction applied. As can be seen in plots a and b, strongly uncorrelated CYGNSS winds have now been flagged out.

TABLE II
BREAKDOWN OF THE NUMBER OF RETRIEVED WIND SPEED SAMPLES IN %

	wind speed range (m/s)	No Flag	Flag on
RCG< 5	0–5	2.68	2.68
	5–10	3.99	3.94
	> 10	2.37	0.16
5≤RCG< 10	0-5	5.36	5.36
	5–10	10.69	10.68
	> 10	2.72	0.81
10≤RCG< 20	0-5	3.90	3.90
	5–10	8.67	8.67
	> 10	0.78	0.61
RCG≥20	0–5	19.32	19.32
	5–10	36.42	36.42
	> 10	3.10	3.07

winds, with a 70% error probability threshold applied, and Fig. 10(d) is the same plot but with the bias correction applied. Finally, Fig. 11 is a repeat of the plots found in Fig. 4, but with both the bias correction and quality flag applied.

Strongly uncorrelated CYGNSS winds, as seen in Fig. 4(a) and (b) are now flagged out, which improve the overall statistics against HWRF. Table II provides a detailed breakdown of the number of retrieved wind speed samples in % for different RCG and wind speed ranges with and without the flag applied. First, we note that 4.37% of the data is filtered out across all RCG ranges. This table also shows that the quality flag mainly impacts higher wind speed retrievals: for wind speeds higher than 10 m/s, 6.73% of the retrievals are retained for RCG less than 5, 29.62% for RCG between 5 and 10, and 79.18% for RCG between 10 and 20. The majority of winds above 10 m/s, with an RCG less than 10 fail to satisfy our performance criteria as defined by (3) and are, therefore, flagged out. However, it is important to note that in the simulated data sample, less than 6% of retrieved winds higher than 10 m/s are observed with low RCG levels. Our analysis indicates the inability of the chosen MV algorithm approach to accurately retrieve winds above 13 m/s for RCG less 10.

III. WIND RETRIEVAL PERFORMANCE IN TROPICAL CYCLONE CONDITION

The available simulated CYGNSS dataset is now compared against TC winds retrieved from a selected airborne (SFMR, GPS dropsondes) and spaceborne (ASCAT, Oceansat-II) sensors, as well as the H*wind model analysis winds. In addition, a maximum wind speed retrieval analysis is also included in this section where we compare the CYGNSS retrieved maximum wind speeds to the national hurricane center (NHC) best track maximum winds (for a given TC, the best track dataset is a postanalysis six-hourly report of several storm parameters including, but not limited to, the center location, atmospheric pressure around the eye, maximum sustained wind speed, and radius of maximum wind).

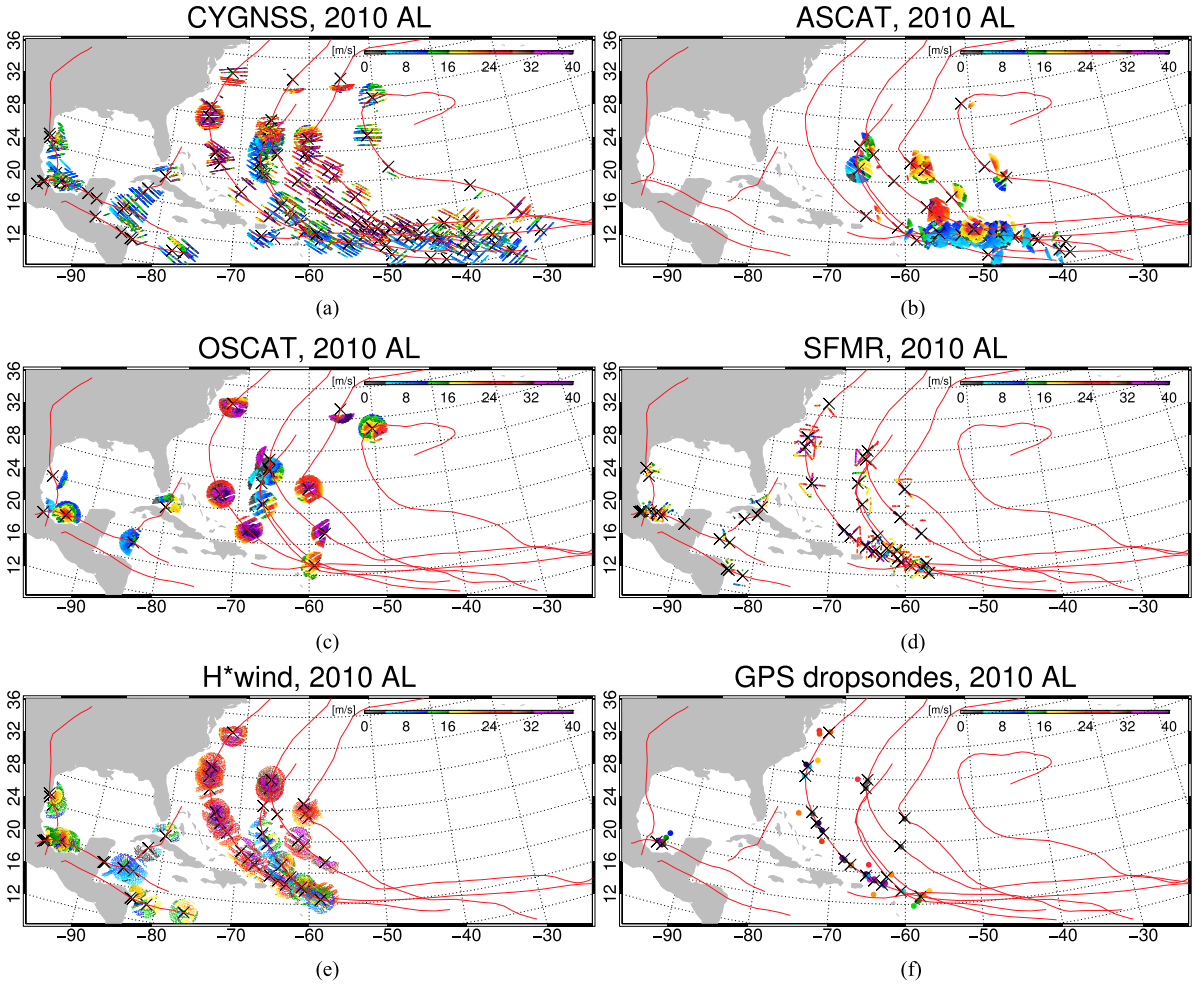

Fig. 12. Retrieved simulated CYGNSS winds for the 2010 hurricane season in the ATL basin are shown in plot a. Retrieved winds from ASCAT, Oceansat-II, SFMR, H*wind, and GPS dropsondes collocated with simulated CYGNSS winds are also shown (see plots b through f). Storm tracks, based on best track data, are shown in red. Note that for adequate visualization, retrieved winds are only shown within a 200-km radius from the various storm eye center locations.

*A. Comparison Against Sensors and the H*wind Model*

Wind speeds retrieved from the ASCAT [19] and the Oceansat-II scatterometer [20], are now compared with CYGNSS winds for the 2010–2011 hurricane seasons in both the ATL and EPAC basins. Wind speeds retrieved from GPS dropsondes [1] as well as the SFMR on board the NOAA WP-3D aircraft [21] are also used as "truth" to validate the CYGNSS wind speed retrievals. Spatial and temporal collocation criteria used for this analysis are 25 km and 3 h, respectively.

Fig. 12(a) shows the retrieved CYGNSS wind speeds over the various TCs from the 2010 hurricane season in the ATL basin; the various storm tracks obtained from the best track data are also included in this plot. Fig. 12(b)–(f) shows retrieved wind speeds from ASCAT, Oceansat-II, SFMR, H*wind, and GPS dropsondes collocated with CYGNSS for the same hurricane season; note that in all of these plots, the wind speed is only plotted within a 200-km radius from the storm center.

Fig. 13 shows a series of scatterplots where the CYGNSS winds are compared against each aforementioned sensor including H*wind for the 2010–2011 hurricane seasons. The first row of scatterplots in Fig. 13 shows the comparison when neither quality flag nor bias correction are applied to the CYGNSS retrieved winds; the second row shows the performance of the CYGNSS retrieved winds with both the quality flag and bias correction applied. Note that the bias correction applied to the CYGNSS winds, in each of these scatterplots, refers to the bias correction generated in Section II-C when comparing the CYGNSS wind speed to HWRF (i.e., we do not attempt to adjust the CYGNSS wind PDF to each of the respective sensor/model wind PDF). As expected, results noticeably improve when both the quality flag and bias correction are applied; the best performance is obtained when compared to the ASCAT, followed by Oceansat-II, with the minimum amount of data flagged.

The CYGNSS baseline performance requirements are defined for wind retrievals over a 25 km × 25 km spatial grid. This resolution condition can only be met when the incidence angle is less than 54.5 degrees (this limitation is a direct result of the instantaneous field of view becoming larger than the required spatial resolution for incidence angles larger than 54.5° [24]). Considering that 24.8% of the simulated measurements were acquired with incidence angles larger than 54.5°, we decided to separate the data into two groups: a high-resolution

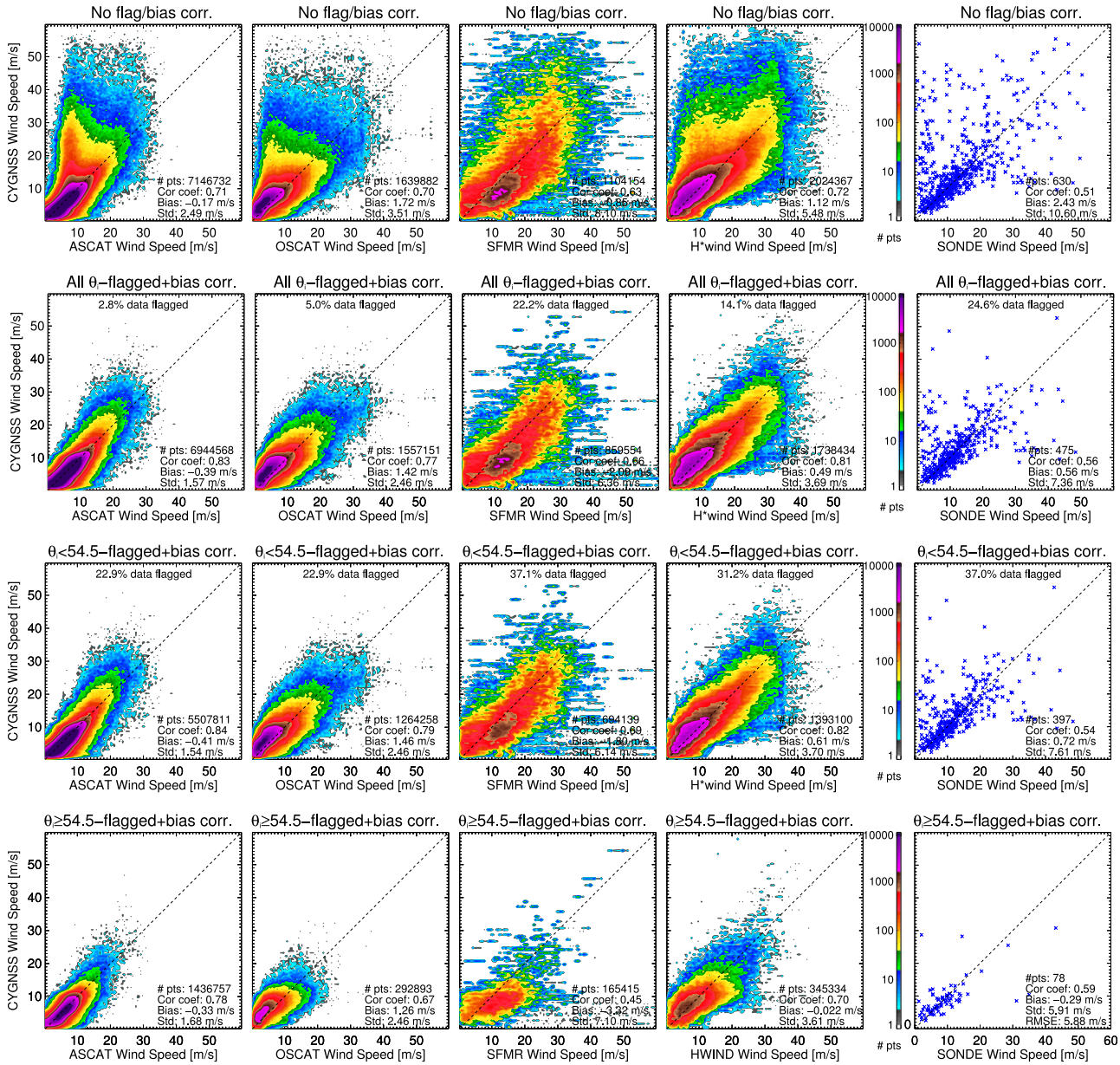

Fig. 13. Scatterplots of simulated CYGNSS winds compared to collocated ASCAT, Oceansat-II, SFMR, H*wind, and GPS dropsondes, for the hurricane seasons 2010-11 in both the ATL and EPAC basins.

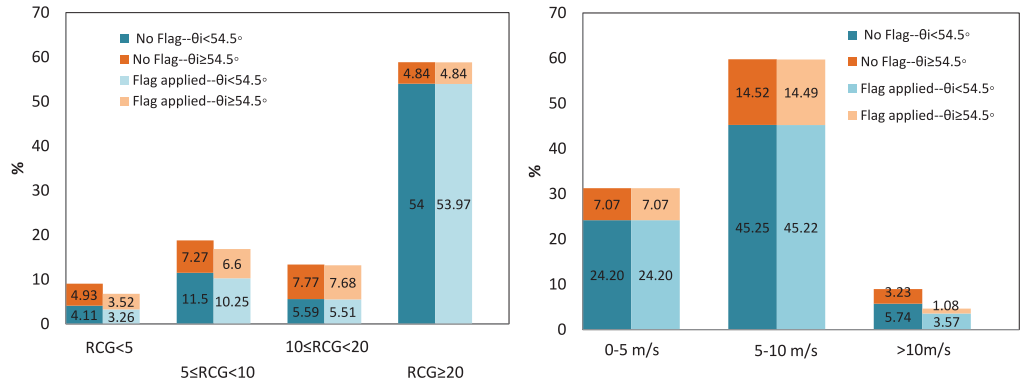

Fig. 14. Distribution of retrieved wind speed samples in % for various RCG and wind speed ranges.

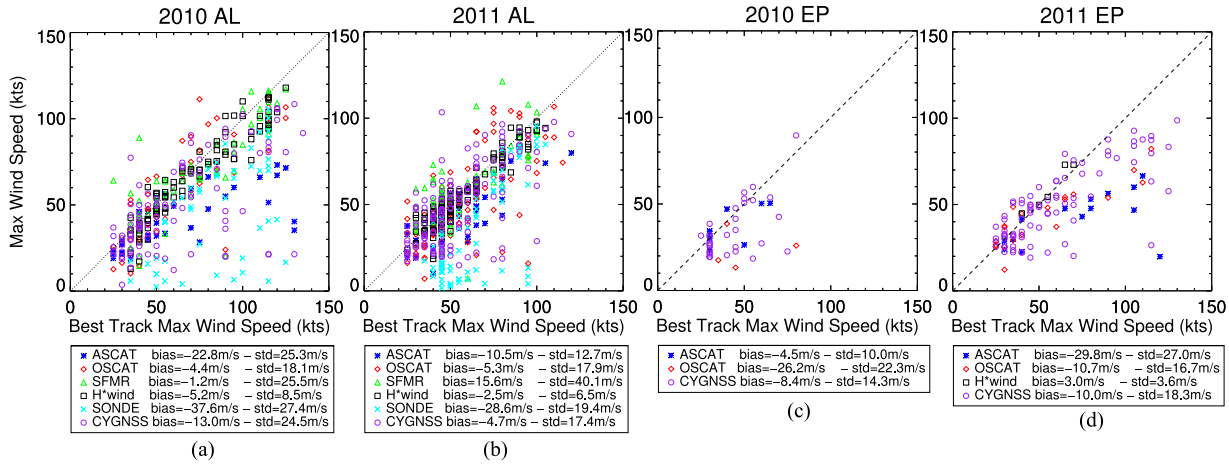

Fig. 15. Scatterplots of simulated CYGNSS maximum winds, including ASCAT, Oceansat-II, SFMR, GPS dropsondes, and H*wind, compared to best track. Each plot represents each sensor and model performance per basin and hurricane season.

set that encompasses all measurements with resolution of up to 25 km (i.e., incidence angles lower than 54.5°), and a low-resolution set which combines all other remaining observations (i.e., incidence angles greater than 54.5°). The distribution of the measurements within these two groups for different RCG and wind speed ranges is presented in Fig. 14. It is important to note that the flag impact is essentially the same for both data groups flagging 2.2% of high-resolution measurements and 2.17% of low-resolution measurements. The third and fourth rows of scatterplots in Fig. 13 shows the CYGNSS retrieved winds in comparison with the same sensors and model for incidence angles less and greater than 54.5°, with both the flag and bias correction applied. The results clearly show that the wind retrieval performance is not degraded when lower resolution measurements are included.

B. Maximum Wind Retrieval Analysis

The NHC routinely reports and forecasts the maximum sustained winds for each monitored TC, which then classifies the given storm (e.g., tropical depression, tropical storm, hurricane). The NHC best track dataset provides this metric every 6 h during the lifetime of a TC. We are interested in comparing the retrieved maximum winds from CYGNSS simulated data, as well as those from the sensors and model used previously, to the NHC best track reported maximum winds. Again, the 2010–2011 hurricane seasons for both the ATL and EPAC basins are used for this exercise.

Fig. 15 shows scatterplots of the retrieved maximum winds from CYGNSS as well as those from ASCAT, Oceansat-II, SFMR, GPS dropsondes, and H*wind, all compared to the best track maximum winds. Each plot shows the results for each respective basin and hurricane season. We first note that the retrieved maximum winds from the H*wind model analysis provides the closest match to the best track for all hurricane seasons and basins. Oceansat-II also performs well compared to best track, with relatively low bias and a consistent standard deviation. However, its performance is poor in the EPAC basin in 2010, which is most likely due to abnormally low storm coverage sampling. The ASCAT, SFMR, and GPS dropsondes winds provide mixed results; ASCAT has high biases and standard deviations for 2010 in the ATL basin, and for 2011 in the EPAC basin, but more acceptable statistics for 2010 in the EPAC basin, and for 2011 in the ATL basin. A closer look at all four plots from Fig. 15 reveals that ASCAT performs well compared to best track up to 60 knots maximum winds. Above this threshold, ASCAT deviates noticeably from best track, which could be attributed to ASCAT not having sampled actual areas of high winds around the storm centers.

Simulated retrieved maximum winds from CYGNSS provide somewhat consistent results, where biases vary between −4.7 down to −13 m/s, and standard deviations varying from 14.3 to 24.5 m/s for all hurricane seasons and basins combined. Although some outliers are clearly noticeable for both hurricane seasons in the ATL basins [see Fig. 15(a) and (b)], CYGNSS appears to be capable of retrieving above 70 knots maximum winds without deviating too much from the best track.

IV. Conclusion

In this paper, we utilized CYGNSS wind observations inferred from simulated CYGNSS measurements to assess the potential of using this instrument in retrieving winds in TC wind conditions. The HWRF model fields from 43 actual TCs from 2010–2011 in both the ATL and EPAC basins were utilized as input to the E2ES to calculate CYGNSS DDMs for these TCs. A GMF and retrieval algorithm, which were developed separately for CYGNSS, were then utilized to retrieve wind speeds. The CYGNSS retrieved winds compared well to HWRF for RCG values greater than 20. However, since only about 59% of the simulated measurements were observed with RCG greater than 20, a quality flag procedure was developed to properly assess wind speed retrieval performance for RCG values less than 20, and to retain as much data as possible without compromising accuracy. The majority of unrealistic wind retrievals occurred for RCG ranges below 10. To filter them

out, we developed and implemented an error probability lookup table. This table reports the probability that a retrieved wind can deviate from the HWRF true winds by more than 2 m/s, given a specific RCG range, a retrieved wind speed from the DDMA observables, and a retrieved wind speed from the LES observables. Using this error probability table, a wind quality flag was defined by applying a 70% error probability threshold to all the retrieved CYGNSS winds. The choice of threshold was determined by balancing the retrieval performance while minimizing the amount of data flagged (up to 4.4%). To further improve the CYGNSS wind speed retrieval performance for moderate to high wind speeds, the PDF matching technique was utilized to determine bias corrections for the CYGNSS wind speed PDF compared to the HWRF wind speed PDF. The biases in the CYGNSS wind speed PDF are probably caused by the combination of shortcomings in the GMF, wind retrieval algorithm, and the E2ES that were employed for this study. We have found that with the currently implemented forward model and MV retrieval algorithm approach, only about 19% of wind speed retrievals above 10 m/s will have adequate accuracy for RCG levels below 10. However, for low wind speed ranges, this algorithm approach is found to be robust for all RCG ranges.

Because actual TCs were utilized in this study, the CYGNSS wind speeds have also been compared to retrievals from several actual wind sources such as ASCAT, Oceansat-II, SFMR, GPS dropsondes, and the H*wind model analysis. When the quality flag and bias correction were applied, the best performance was obtained when compared to the ASCAT sensor, with an overall bias around -0.4 m/s and standard deviation less than 1.54 m/s. The worse performance was observed when simulations were compared to GPS dropsondes; overall standard deviation was around 7.36 m/s, but overall bias remained small (0.56 m/s). The temporal and spatial averaging scales are quite different so these results were not that surprising given the relatively small dataset. Finally, the CYGNSS capability to retrieve the TC maximum wind was evaluated using the NHC best track maximum winds for the same set of TCs. Although the CYGNSS overall bias varied from season to season (from -4.7 m/s in the ATL basin-2011 to -13.0 m/s in the ATL basin-2010), the standard deviation stayed fairly consistent for most seasons (14.3–17.4 m/s), except in the ATL basin in 2010 (24.5 m/s). The large range of maximum wind variations is probably due to the simulated sensor track missing the region of maximum winds. Because the NHC best track database does not give the precise location of the maximum winds relative to the center position of a given TC, this variability is difficult to quantify. This study illustrates the potential of CYGNSS to retrieve sea surface wind speeds in the TC environment. While there are obvious limitations in any simulated dataset, a similar methodology will be followed once actual CYGNSS measurements become available. Future work will also include refinement of the forward model and investigation of the impacts of ancillary ocean parameters such as the mean square slope and the significant wave height. Additionally, the DDM data from the recently launched SGR ReSi GNSS receiver onboard TechDemoSat-1, which shares similarities with CYGNSS, will also be analyzed to help assess CYGNSS performance prior to launch.

APPENDIX

The RCG is defined as

$$\mathrm{RCG} = \frac{G_{Rx}^{Sp}}{(R_{TxSp}R_{RxSp})^2} \tag{5}$$

where G_{Rx}^{SP} represents the receiver antenna gain (numeric) at the specular point, R_{TxSp} is the distance (in meters) between the GPS transmitter and the specular point on the earth surface, and R_{RxSp} is the distance (in meters) between the CYGNSS receiver antenna and the specular point on the earth surface [24]. Although the RCG unit is technically m^{-4}, we have decided to leave the RCG unitless throughout the manuscript.

REFERENCES

[1] T. F. Hock and J. L. Franklin, "The NCAR GPS dropwindsonde," *Bull. Amer. Meteorological Soc.*, vol. 80, no. 3, pp. 407–420, Mar. 1999.

[2] F. M. Naderi, M. H. Freilich, and D. G. Long, "Spaceborne radar measurement of wind velocity over the ocean—An overview of the NSCAT scatetterometer system," *Proc. IEEE*, vol. 79, no. 6, pp. 850–866, Jun. 1991.

[3] M. J. Brennan, C. C. Hennon, and R. D. Knabb, "The operational use of QuikSCAT ocean surface vector winds at the national hurricane center," *Weather Forecasting*, vol. 24, pp. 621–645, Jun. 2009.

[4] B. Candy, S. English, and S. Keogh, "A comparison of the impact of quikscat and windsat wind vector products on met office analyses and forecasts," *IEEE Trans. Geosci. Remote Sens.*, vol. 47, no. 6, pp. 1632–1640, Jun. 2009.

[5] J. Ahn, Z. Jelenak, J. Sienkiewicz, and M. Brennan, "Ocean surface winds from space—A collaborative education effort," in *Proc. OCEANS*, Sep. 2006, pp. 1–6.

[6] F. Monaldo, C. Jackson, and W. Pichel, "Seasat to RADARSAT-2: Research to operations," *Oceanography*, vol. 26, no. 2, pp. 34–45, 2013. [Online]. Available: http://dx.doi.org/10.5670/oceanog.2013.29

[7] V. Zavorotny and A. Voronovich, "Scattering of GPS signals from the ocean with wind remote sensing application," *IEEE Trans. Geosci. Remote Sens.*, vol. 38, no. 2, pp. 951–964, Mar. 2000.

[8] V. Zavorotny, S. Gleason, E. Cardellach, and A. Camps, "Tutorial on remote sensing using GNSS bistatic radar of opportunity," *IEEE Geosci. Remote Sens. Mag.*, vol. 2, no. 4, pp. 8–45, Dec. 2014.

[9] A. Komjathy, M. Armatys, D. Masters, P. Axelrad, V. Zavorotny, and S. Katzberg, "Retrieval of ocean surface wind speed and wind direction using reflected GPS signals," *J. Atmos. Oceanic Technol.*, vol. 21, pp. 515–526, 2004.

[10] S. J. Katzberg, O. Torres, and G. Ganoe, "Calibration of reflected gps for tropical storm wind speed retrievals," *Geophysical Res. Lett.*, vol. 33, no. 18, 2006, Art. no. l18602. [Online]. Available: http://dx.doi.org/10.1029/2006GL026825

[11] M. P. Clarizia, C. P. Gommenginger, S. T. Gleason, M. A. Srokosz, C. Galdi, and M. Di Bisceglie, "Analysis of gnss-r delay-doppler maps from the uk-dmc satellite over the ocean," *Geophysical Res. Lett.*, vol. 36, no. 2, 2009, Art. no. l02608. [Online]. Available: http://dx.doi.org/10.1029/2008GL036292

[12] S. J. Katzberg, J. Dunion, and G. G. Ganoe, "The use of reflected GPS signals to retrieve ocean surface wind speeds in tropical cyclones," *Radio Sci.*, vol. 48, no. 4, pp. 371–387, 2013. [Online]. Available: http://dx.doi.org/10.1002/rds.20042

[13] P. Jales and M. Unwin, "Mission description - GNSS reflectometry on TDS-1 with the SGR-ReSI," Surrey Satellite Technology Ltd, Guildford, U.K., Tech. Rep. 0248367 Revision 001, 2015.

[14] G. Foti, C. Gommenginger, P. Jales, M. Unwin, A. Shaw, C. Robertson, and J. Rosell, "Spaceborne gnss reflectometry for ocean winds: First results from the uk techdemosat-1 mission," *Geophysical Res. Lett.*, vol. 42, no. 13, pp. 5435–5441, 2015. [Online]. Available: http://dx.doi.org/10.1002/2015GL064204

[15] C. Ruf *et al.*, "Cygnss: Enabling the future of hurricane prediction [remote sensing satellites]," *IEEE Geosci. Remote Sensing Mag*, vol. 1, no. 2, pp. 52–67, Jun. 2013.

[16] C. Ruf, A. Lyons, and A. Ward, "NASA Intensifies Hurricane Studies with CYGNSS," *Earth Observer, NASA*, vol. 25, no. 3, pp. 12–21, May/Jun. 2013.

[17] A. O'Brien, End-to-end simulator technical memo (No. 148-0123, Revision 0, Initial Release), Jan. 2014, University of Michigan, Ann Arbor, MI, USA, Unpublished internal document.
[18] M. Clarizia, C. Ruf, P. Jales, and C. Gommenginger, "Spaceborne gnss-r minimum variance wind speed estimator," *IEEE Trans. Geoscience Remote Sensing.*, vol. 52, no. 11, pp. 6829–6843, Nov. 2014.
[19] *ASCAT Product Guide*. EUMETSAT, Eumetsat-Allee 1, D-64295 Darmstadt, Germany. (2015, Jul). [Online]. Available: http://www.eumetsat.int/website/home/Data/RegionalDataServiceEARS/EARSA SCAT/index.html
[20] SCAT-DP Team, *Oceansat-2 Scatterometer Algorithms for Sigma-0, Processing and Products Format*, Space Applications Centre, Ahmedabad, Gujarat, India, Apr. 2010.
[21] E. W. Uhlhorn, P. G. Black, J. L. Franklin, M. Goodberlet, J. Carswell, and A. S. Goldstein, "Hurricane surface wind measurements from an operational stepped frequency microwave radiometer," *Monthly Weather Rev.*, vol. 135, no. 9, pp. 3070–3085, Sep. 2007.
[22] M. D. Powell, S. H. Houston, L. R. Amat, and N. Morisseau-Leroy, "The HRD real-time hurricane wind analysis system," *J. Wind Eng. Ind. Aerodynamics*, vol. 77–78, pp. 53–64, 1998.
[23] D. S. Nolan, R. Atlas, K. T. Bhatia, and L. R. Bucci, "Development and validation of a hurricane nature run using the joint osse nature run and the wrf model," *Journal J. Adv. Modeling Earth Syst.*, vol. 5, no. 2, pp. 382–405, 2013. [Online]. Available: http://dx.doi.org/10.1002/jame.20031
[24] M. P. Clarizia and V. Zavorotny, Algorithm theoretical basis document: Level 2 wind speed retrieval (No. 148-0138, Revision 2, Change 2), Nov. 2015, University of Michigan, Ann Arbor, MI, USA, Unpublished internal document.
[25] V. Tallapragada, L. Bernardet, S. Gopalakrishnan, Y. Kwon, Q. Liu, T. Marchok, D. Sheinin, M. Tong, S. Trahan, R. Tuleya, R. Yablonsky, and X. Zhang, *Hurricane Weather and Research and Forecasting (HWRF) Model: 2013 Scientific Documentation*, Aug. 2013.
[26] F. J. Wentz and D. K. Smith, "A model function for the ocean-normalized radar cross section at 14 ghz derived from nscat observations," *J. Geophysical Res.: Oceans*, vol. 104, no. C5, pp. 11499–11514, 1999. [Online]. Available: http://dx.doi.org/10.1029/98JC02148

Faozi Saïd (S'07–M'15) received the M.Sc. degree in electrical engineering from Brigham Young University, Provo, UT, USA, in 2009, and the Ph.D. degree in physics from the University of Tromsø, Tromsø, Norway, in 2015.

From 2012 to 2014, he was also a Guest Research Scientist at the Spatial Oceanography Laboratory, French Research Institute for Exploitation of the Sea in Brest, France. He is currently working for Global Science & Technology, Inc. as a Support Scientist with the Ocean Surface Winds Team at the Center for Satellite Application and Research (STAR), National Environmental Satellite Data and Information Service, National Oceanic and Atmospheric Administration. His current research interests include sea surface wind retrievals from both active and passive microwave remote sensing instruments including, but not limited to, the RapidScat and the upcoming NASA cyclone global navigation satellite system mission.

Seubson Soisuvarn (S'02–M'07) received the B.Eng. degree in electrical engineering from Kasetsart University, Bangkok, Thailand, in 1998, and the Ph. D. degree in electrical engineering from the University of Central Florida, Orlando, FL, USA, in 2006.

Since 2006, he has been with the Ocean Surface Winds Team as a UCAR Visiting Scientist at the Center for Satellite Applications and Research, National Environmental Satellite, Data, and Information Service, National Oceanic and Atmospheric Administration. His interests include active and passive microwave remote sensing and GNSS Reflectometry of the ocean surface and wind retrieval algorithm development. He has worked on calibration and validation of scatterometers data including ASCAT and Oceansat-2 and has developed the high wind geophysical model function (CMOD5.H) for C-band scatterometer that is using operationally by the National Weather Service. He is currently working on calibration and validation of the NASA cyclone global navigation satellite system mission.

Zorana Jelenak (S'97–M'04) received the Ph.D. degree in physics from Waikato University, Hamilton, New Zealand, in 2000.

She joined Ocean Winds Team at NOAA/NESDIS/ORA as a UCAR visiting scientist in March 2001. She is a Member of the NASA Ocean Surface Winds science team, NOAA's EDR algorithm lead for AMSR-2 radiometer and a Member of NASA CYGNSS science team. Her interests include ocean surface wind vector measurements from active and passive microwave measurements and its applicability in an operational near-real time environment, retrieval algorithm development, model function development, advanced statistical analysis, and error analysis for improved algorithm characterization.

Paul S. Chang received the B.S. degree in electrical engineering from Union College, Schenectady, NY, USA, in 1988, and the Ph.D. degree in electrical engineering in 1994 from the University of Massachusetts, Amherst, MA, USA.

Since 1994, he has been a Research Physical Scientist at the Center for Satellite Applications and Research, National Environmental Satellite, Data and Information Service (NESDIS), National Oceanic and Atmospheric Administration (NOAA). His current activities include research and development in active and passive microwave remote sensing of the ocean surface with and emphasis on retrieval of the ocean surface wind field. Wind retrieval algorithm improvements and new product developments are pursued through the analyses of satellite and aircraft microwave remote sensing data. An emphasis is placed on transitioning research results into operational use, which involves cooperative relationships with the operational facets of NESDIS and with the National Weather Service, a primary end user of this data. His current efforts are focused on working on the METOP, RapidScat, CYGNSS, and GCOM-W missions in addition to planning and risk reduction activities for future ocean vector winds missions.